Vietnam Journal of Chemistry, International Edition, **55**(2): 139-147, 2017
DOI: 10.15625/2525-2321.2017-00433

A fluorescent chemodosimeter based on rhodamine derivative for detection of Hg(II) ions studied by using the density functional theory

Phan Tu Quy[1,2], Nguyen Khoa Hien[3], Truong Quy Tung[4], Duong Tuan Quang[5*]

[1]*Department of Chemistry - Hue University of Sciences - Hue University, Hue City, 84-54, Vietnam*

[2]*Tay Nguyen University, Buon Ma Thuot City, 84-50, Vietnam*

[3]*Mientrung Institute for Scientific Research - Vietnam Academy of Science and Technology, Hue City, 84-54, Vietnam*

[4]*Hue University, Hue City, 84-54, Vietnam*

[5]*Department of Chemistry - Hue University of Education - Hue University, Hue City, 84-54, Vietnam*

Received 7 November 2016; Accepted for publication 11 April 2017

Abstract

The synthesis, characteristics and applications of the rhodamine derivative-based fluorescent chemodosimeter **RT** for detection of mercury ions have been studied at the B3LYP/LanL2DZ level of theory. The calculated results confirmed the presence of spirolactam ring in **RT** molecule. The Hg(II) ions reacted with **RT** to form **RG**, accompanied by the formation of guanidine ring and the spirolactam ring-opening in **RG**, turning on the fluorescence of **RG**. These results were in a good agreement with experimental investigations. It indicated that the quantum chemical calculations could be used well for the design, synthesis of the fluorescent chemodosimeter.

Keywords. Fluorescence, chemodosimeter, rhodamine, mercury, DTF, TD-DFT.

1. INTRODUCTION

The fluorescent sensors (chemodosimeter and chemosensor) are molecular sensors based on the transforms of fluorescence signal resulting in the interaction of the analytes with sensors. The first chemodosimeter based on spirolactam ring-opening process of rhodamine B derivative for the detection of Cu(II) ions was reported by Czarnik (1992) [1]. The publications of new fluorescent sensors have rapidly increased since 2005. Nowadays, new fluorescent sensors have been reported almost every week in the world [2]. This is due to the fact that the fluorescent sensors are often sensitive to the analytes, easy to carry out, and less expensive [3]. The fluorescent sensors are studied and applied for detecting many different objects, especially heavy metal ions.

A great number of fluorescent sensors have recently been reported and can be used to selectively detect many different heavy metals ions, such as Hg(II), Cu(II), Fe(II), Fe(III), and Al(III) [4-8]. Many fluorescent sensors can detect metal ions in living cells like Fe(III) in Hepatic cells, Cu(II) in HepG2 cells [4], Hg(II) in PC3 cells [7], etc. However, the development of new fluorescent sensors for detection of trace heavy metal ions in various objects is currently receiving considerable attention due to their increasingly serious pollution. Scientists still continue to develop new fluorescent sensors to improve the detection limit, the selectivity, the solubility, the pH working range, the excitation and emission wavelength, etc [9-13].

The reported fluorescent sensors for the detection of heavy metal ions, biothiols and other analytes are studied mainly by experimental methods (including the design, synthesis, and application) and based on the researcher's experience [14, 15].

Currently, quantum chemical calculation can predict or explain many important properties of chemical systems [16, 17]. Using the quantum chemical calculation to study the synthesis and applications of fluorescent sensors is very useful, helping us to understand the nature of processes to provide a basis for research and development of new sensors. In this work, following the previously reported experimental studies [12], the synthesis process, characteristics and applications of a fluorescent chemodosimeter based on a rhodamine derivative for detection of Hg(II) ions were studied

at the B3LYP/LanL2DZ level of theory with a combination of AIM and NBO analysis.

2. MATERIALS AND METHODS

2.1. Instruments

^{1}H NMR spectra were obtained on Bruker-400 instrument (400 MHz); mass spectra were acquired on Finnigan 4021C MS-spectrometer; elemental analysis was carried out on Flash EA 1112 instrument; UV-Vis spectra and fluorescence spectra were performed on Shimadzu UV-1800 UV-Vis spectrophotometer and Shimadzu RF-5301 PC series fluorescence spectrometer, respectively.

2.2. Reagents

4-nitrophenyl isothiocyanate, rhodamine 6G, ethylenediamine, and all cations (Zn^{2+}, Cu^{2+}, Cd^{2+}, Pb^{2+}, Ag^{+}, Fe^{2+}, Cr^{3+}, Co^{3+}, Ni^{2+}, Ca^{2+}, Mg^{2+}, K^{+} and Na^{+}) were obtained from Aldrich. Acetonitrile, ethanol, and all other solvents were HPLC-grade reagents without fluorescent impurity.

2.3. Computational methods

Geometry optimization and single point energy calculations of molecules were carried out using density functional theory (DFT) with the Gaussian 09 program. The B3LYP density function was applied using the LanL2DZ basis set [17-19].

The variation of enthalpy (ΔH^{298}) and variation of Gibbs free energy (ΔG^{298}) of reactions (at 1.0 atmosphere and 298K) are calculated based on the difference between the total energy of the reaction products and the total energy of the reactants, with the following equations [19]:

$$\Delta H^{298} = \Sigma(\varepsilon_0 + H_{corr})_{\text{products}} - \Sigma(\varepsilon_0 + H_{corr})_{\text{reactants}}$$
$$\Delta H^{298} = \Sigma(\varepsilon_0 + G_{corr})_{\text{products}} - \Sigma(\varepsilon_0 + G_{corr})_{\text{reactants}}$$

Where ε_0 is total energies of the molecule, H_{corr} and G_{corr} are the thermal correction to enthalpy and the thermal correction to Gibbs free energy.

The excited state and time-dependent factors were investigated using time-dependent density functional theory (TD-DFT) at the same level of theory [11]. Topological properties of electron density were probed using the AIM 2000 software for the atom-in-molecule (AIM) theory. The characteristics of each bond critical point (BCP) and bond ring critical point (RCP) considered in this study included the electron density ($\rho(r)$), its Laplacian ($\nabla^2(\rho(r))$ [11, 20-21]. Those theoretical calculations were carried out on a supercomputer operating system with a 32-cores processor and 72-gigabytes memory at the laboratory of computational chemistry and modelling of Quy Nhon University.

3. RESULTS AND DISCUSSION

3.1. The survey on the calculation method

To use the B3LYP/LanL2DZ level of theory for research compounds, a comparison between the calculated results and the experimental structure of rhodamine (fluorophore) has been carried out. The optimized geometry of rhodamine with the numbering scheme of the atoms is shown in Fig. 1. The calculated and experimental bond lengths in rhodamine were listed in table 1.

Table 1: The calculated and experimental bond lengths in rhodamine (Å)

Bond lengths	Exp [23]	B3LYP
C1-C2	1.442	1.419
C1-C6	1.341	1.390
C1-C21	1.502	1.510
C2-C3	1.409	1.401
C2-N22	1.325	1.408
C3-C4	1.361	1.387
C4-C5	1.419	1.406
C4-O7	1.368	1.363
C5-C6	1.430	1.407
C5-C10	1.388	1.448
C10-C15	1.491	1.495
C15-C16	1.400	1.412
C15-C20	1.381	1.402
C16-C17	1.392	1.402
C16-C29	1.475	1.501
C17-C18	1.361	1.388
C18-C19	1.370	1.393
C19-C20	1.373	1.392
N22-C27	1.455	1.473
C27-C28	1.493	1.523
C29-O30	1.193	1.212
C29-O31	1.333	1.342
O31-C33	1.462	1.453
C32-C33	1.470	1.519

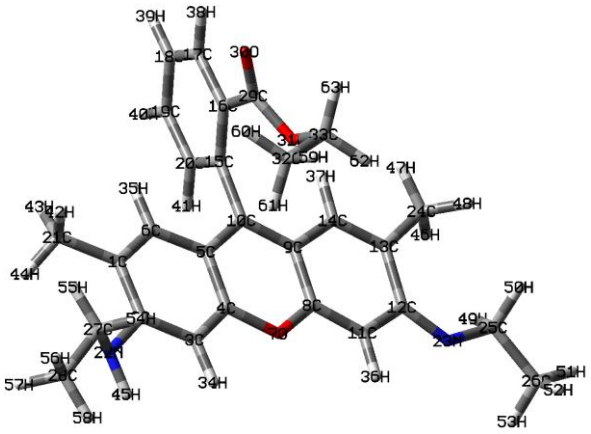

Figure 1: The optimized geometry of rhodamine at the B3LYP/LanL2DZ level of theory

The paired t-test method in the statistical test was used for comparison between the calculated values and experimental values [23]. For the bond length, the calculated value of $|t|$ of 0.54 is less than the critical value of $|t|$ of 2.07 (f = n-1 = 23 degrees of freedom, P = 0.05). These results indicate that the difference between the calculated and experimental values is insignificant. Therefore, the selected level of theory is possible to apply to the research system with reliable results.

3.2. The synthesis and characterization of sensor

The sensor **RT** (rhodamine-ethylenediamine-nitrothiourea conjugate) was synthesized via two reactions. The synthetic procedure of the **RT** is shown in figure 2. The calculated enthalpies (ΔH^{298}) and free energies (ΔG^{298}) of reactions at the B3LYP/LanL2DZ level are summarized in table 2. The obtained results indicate that the enthalpies and free energy of these reactions are quite negative. This indicates that the reactions (1) and (2) are energetically favorable.

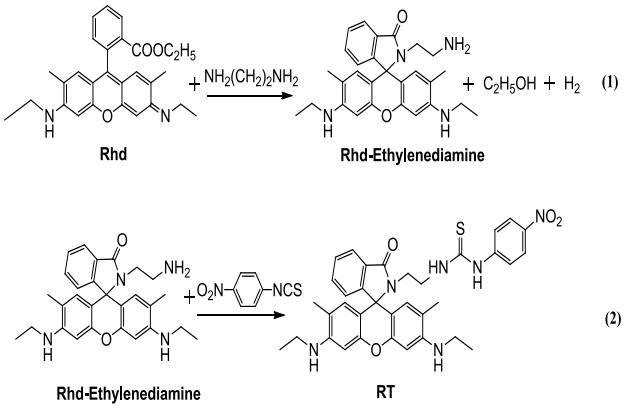

Figure 2: Synthetic procedure of the **RT**

Table 2: The calculation results of enthalpies and free energies of reactions at the B3LYP/LanL2DZ level (kcal.mol^{-1})

Reaction	ΔH^{298}	ΔG^{298}
(1)	-757.9	-765.1
(2)	-25.1	-6.3

The synthesis of **RT** was studied and presented in our previous publication [12]. Accordingly, the chemodosimeter **RT** was synthesized from the reaction of the rhodamine 6G and ethylenediamine, followed by the reaction with 4-nitrophenyl isothiocyanate in *ca.* 39.5 % overall yield. The structures of intermediate and final products were confirmed by ^{1}H NMR and mass spectra. The structure of **RT** was obtained as shown in figure 2.

The optimized geometry of **RT** with the numbering scheme of the atoms is identified at the B3LYP/LanL2DZ level of theory and is shown in figure 3. The theoretical structural parameters such as bond lengths, bond angles and dihedral angles of **RT** are shown in table 3. The obtained results show that the majority of the atoms in the **RT** molecule is distributed on two perpendicular planes. The C2–C12–N19–C25 dihedral angle in **RT** is 85.2^0. One of them contains the C1, C2, C3, C4, C5, C6, N7, C8, C9, C10, C11, C12, C13, C14, C15, N16, N17, and C18 atom. The other one contains the N19, C20, C21, C22, C23, C24, C25 and C26 atoms.

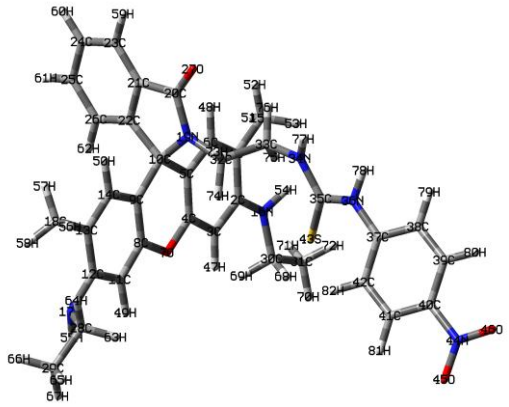

Figure 3: The optimized geometry of **RT** with the numbering scheme of the atoms at the B3LYP/LanL2DZ level of theory

The C5–C9–N19–C22 dihedral angle in **RT** is 73.1^0. The C5–C10–C9, C5–C10–C22, C9–C10–N19, C9–C10–C22 angles are 110.2^0, 112.2^0, 110.6^0, 112.0^0, respectively. The C5–C10–C9, C5–C10–C22, C9–C10–N19, C9–C10–C22 angles are 110.2^0, 112.2^0, 110.6^0, 112.0^0, respectively. The C5–C10, C9–C10, C22–C10 bond lengths are 1.522 Å, 1.525

Å, 1.530 Å, nearly the same as the C–C single bond (1.5 Å). The C10–N19 bond length is 1.496 Å, nearly the same as the C–N single bond (1.5 Å). The results show that the C10 atom acquires sp^3 hybrid state.

The N19, N34, N36, N44 atoms acquire sp^3 hybrid state, but the N19–C10–C20–C32, N34–C33–C35–H77, N36–C35–C37–H78, N44–C40–O45–O46 dihedral angles are 3.6^0, 6.8^0, 6.3^0, 0.1^0, respectively, different from the N-H-H-H dihedral angle of 35^0 in NH_3.

The structure of **RT** was again confirmed by the results obtained from AIM analysis. The calculated values of $\rho(r)$ and $\nabla^2(\rho(r))$ at the BCPs of **RT** are listed in table 4. The topological properties of the BCPs are summarized in Fig. 4a.

The results obtained from AIM analysis also indicate the presence of the BCPs in each of the intermolecular contacts in **RT**, especially at the new bonds formed. A RCP is found in the central area of the C10, N19, C20, C21 and C22 atom, indicating the presence of spirolactam ring in **RT**. The molecular structure of **RT** obtained from the theoretical investigations agrees well with experimental results as shown in figure 2.

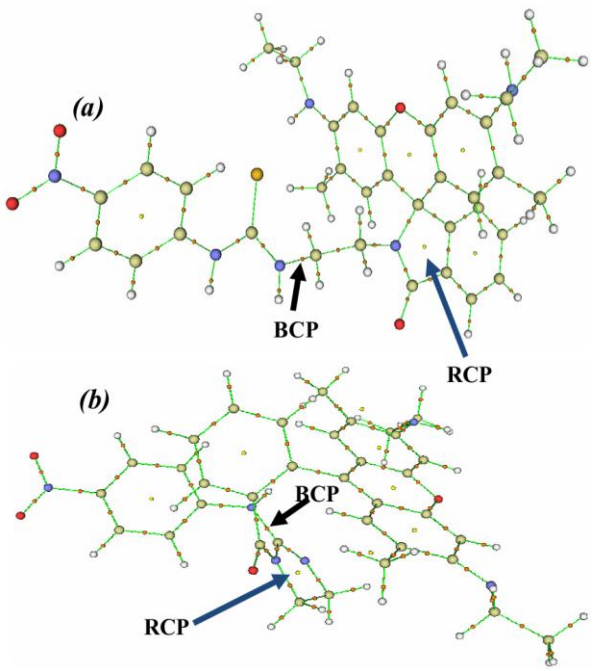

Figure 4: The topological properties of **RT** (a) and **RG** (b), at the Bond Critical Points (BCPs) and Ring Critical Point (RCPs): Bond Critical Points (BCPs) denoted by red color, Ring Critical Points (RCPs) denoted by yellow color

Table 3: The structural parameters of **RT**, bond lengths in angstrom, angles in degrees

Bond lengths	B3LYP	Bond angles	B3LYP	Dihedral angles	B3LYP
C1–C2	1.425	C1–C2–C3	118.9	C1–C2–C3–C4	-0.1
C2–C3	1.396	C4–O7–C8	118.9	C3–C4–O7–C8	179.9
C4–N7	1.373	C5–C10–C9	110.2	C5–C10–C9–C14	-178.6
N7–C8	1.370	C9–C10–N19	110.6	O7–C8–C11–C12	-179.7
C8–C9	1.392	C5–C10–C22	112.2	C4–C5–C10–N19	121.3
C9–C10	1.525	C22–C10–N19	100.1	C9–C10–C22–C26	-63.8
C5–C10	1.522	C10–N19–C20	114.3	C9–C10–N19–C20	-116.5
C8–C11	1.395	N19–C20–O27	125.4	C10–N19–C20–C21	-1.8
C10–N19	1.496	C21–C20–O27	128.5	C10–N19–C20–O27	178.1
C10–C22	1.530	C22–C21–C23	121.8	O27–C20–N19–C32	3.8
C20–N19	1.373	C20–N19–C32	121.3	C20–N19–C32–C33	-78.0
C20–C21	1.486	N19–C32–C33	112.1	N19–C32–C33–N34	167.0
C21–C22	1.390	C32–C33–N34	112.3	C32–C33–N34–C35	87.5
C20–O27	1.224	C33–N34–C35	125.6	C33–N34–C35–N36	176.1
N19–C32	1.451	N34–C35–N36	111.4	C33–N34–C35–S43	-1.5
C32–C33	1.541	N34–C35–S43	123.5	N34–C35–N36–C37	170.0
C33–C34	1.458	S43–C35–N36	125.1	C35–N36–C37–C38	154.2
N34–C35	1.360	C35–N36–C37	130.8	C37–C38–C39–C40	0.3
C35–S43	1.670	C37–C38–C39	121.0	C39–C40–N44–O45	-179.3
C35–N36	1.391	C40–N44–O45	117.8	C39–C40–N44–O46	0.7

Bond lengths	B3LYP	Bond angles	B3LYP	Dihedral angles	B3LYP
N36–C37	1.401	C40–N44–O46	117.8	C4–C3–C2–N16	-178.4
C37–C38	1.406	O45–N44–O46	124.4	C8–C11–C12–N17	177.0
C40–N44	1.468			C2–N16–C30–C31	-175.8
N44–O45	1.227			C12–N17–C28–C29	179.4
N44–O46	1.228				

Table 4: Electron density (*ρ(r)*, in au) and the Laplacian ($\nabla^2(\rho(r))$, in au) of **RT** and **RG** at the B3LYP/LanL2DZ level of theory

Compound	Bond	ρ(r)	λ_1	λ_2	λ_3	$\nabla^2(\rho(r))$	Critical Point
RT	N34···C35	0.300	4.544	-1.278	-3.239	0.249	BCP
	C10···N19···C20···C21···C22	0.042	-5.676	-0.178	-3.566	0.163	RCP
RG	N22···C23	0.272	-1.019	-1.188	-3.153	0.249	BCP
	N22···C23···N24···C25···C26	0.045	0.133	-1.029	-4.565	0.163	RCP

3.3. The application of sensor

The previously published experimental results indicated that **RT** could be used as a fluorescent chemodosimeter for selective detection of Hg(II) ions in water media in the presence of the competing metal ions. The addition of Hg(II) ions to the aqueous solution of the chemodosimeter **RT** caused an irreversible fluorescence *OFF-ON* response with a remarkable visual color change from colorless to pink. The experimental results suggested that the addition of Hg(II) induced a desulfurization reaction and cyclic guanylation of thiourea moiety followed by the ring-opening of rhodamine spirolactam in **RT**, finally, a new rearrangement product **RG** was formed as shown in figure 5. This led to the change in fluorescence signal [12].

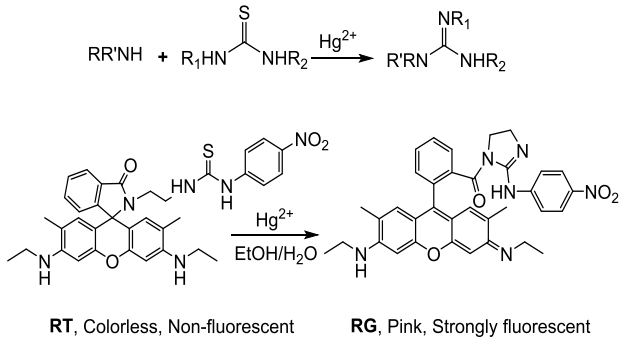

Figure 5: The proposed mechanism of the reaction between **RT** and Hg(II) ions

To shed light on the cause of the fluorescence signal changes in the reaction between Hg(II) ions and **RT** to form **RG**, the theoretical investigation on the optimized geometry of the ground state, excited states, AIM and NBD analysis have been conducted for both **RT** and **RG**.

The optimized geometry of **RG** (with the numbering scheme of the atoms) is identified at the B3LYP/LanL2DZ level of theory and is shown in figure 6. The calculated values of *ρ(r)* and $\nabla^2(\rho(r))$ at the BCPs of **RG** are listed in table 3. The topological properties of the BCPs are summarized in figure 4b. The results obtained from AIM analysis confirms the presence of bonds through the presence of the BCPs in each of the intermolecular contacts in **RG**, especially at the new bonds formed or the new

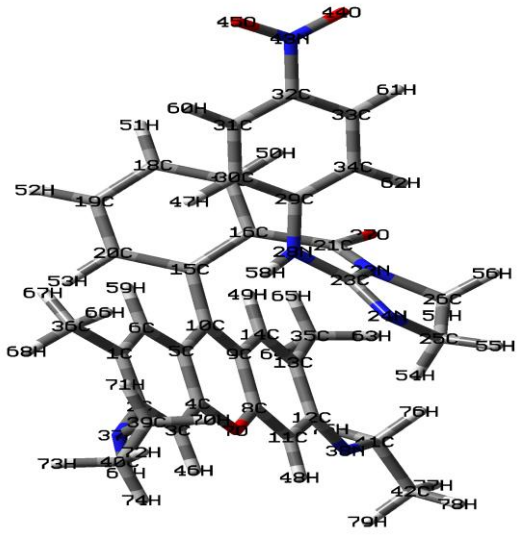

Figure 6: The optimized geometry of **RG** with the numbering scheme of the atoms at the B3LYP/LanL2DZ level of theory

bonds cleaved. The results obtained from AIM analysis show the presence of a RCP in the central area of the N22, C23, N24, C25, and C26 atom. There is not any RCP in the central area of the C10, C15, C16, C21, N22 and O27 atom in RG, suggesting the presence of guanidine ring, and the absence of spirolactam ring in **RG**. These theoretical investigations agree well with experimental results as shown in figure 5.

The UV-Vis spectra, the electronic and fluorescent properties of **RT** and **RG** were calculated using the TD-DFT method at the same level optimized structure. Fig. 7 shows that **RT** exhibits a characteristic absorption band at 543.6 nm with a insignificant oscillation strength of 0.0003. Meanwhile, **RG** exhibits a characteristic absorption band at 476.5 nm with strong oscillation strength of 0.5727. These calculated results are quite similar to the experimental investigations.

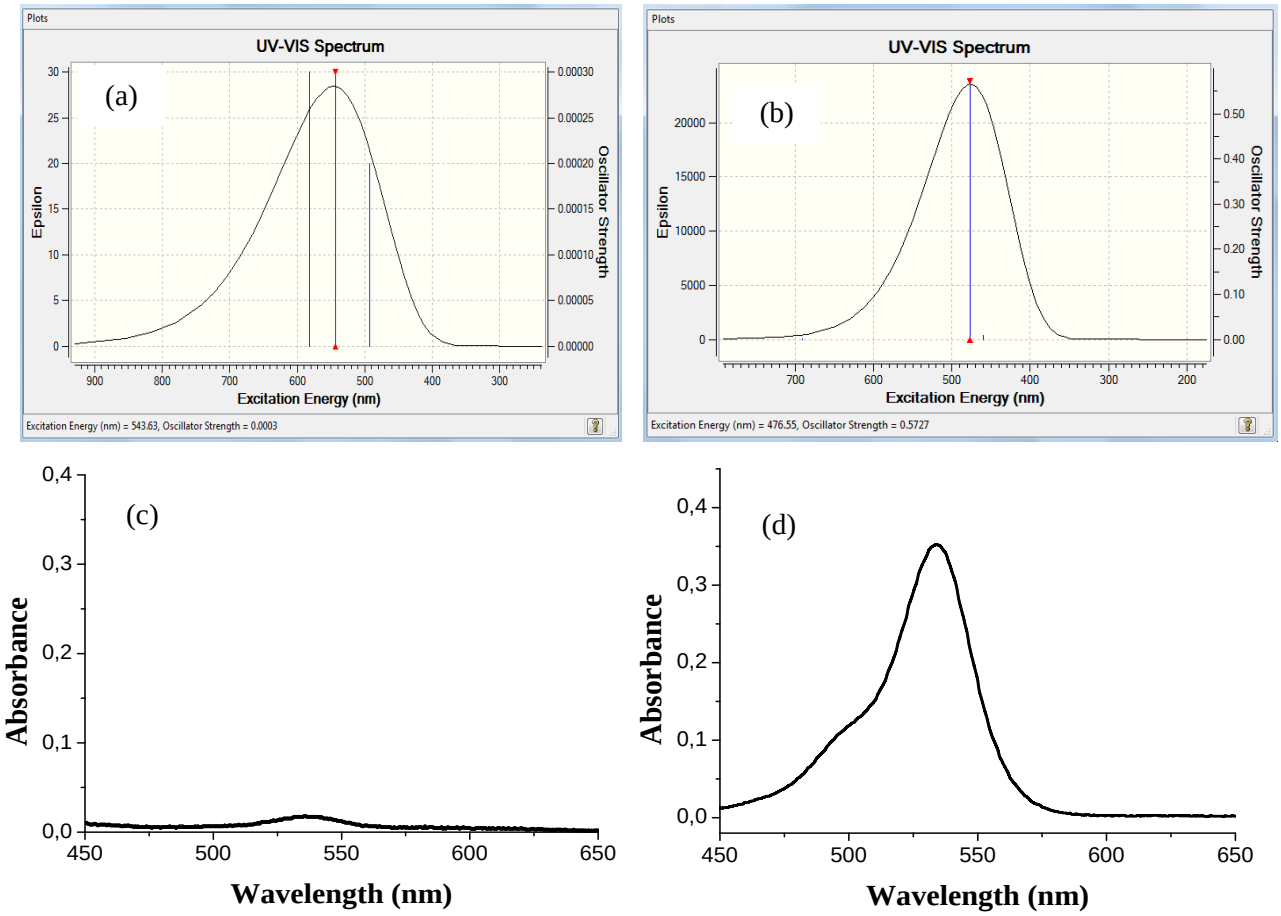

Figure 7: The UV-Vis spectra of **RT** (a) and **RG** (b) at the B3LYP/LanL2DZ level of theory
The UV-Vis experimental spectra of **RT** (c) and **RG** (d).

Table 5: Calculated excitation energy (*E*), wavelength (λ), and oscillator strength (*f*) for low-laying singlet state of **RT** and **RG**

Compound		Main orbital transition	TD-DFT/B3LYP/LanL2DZ CIC[a]	*E*(eV)	λ(nm)	*f*
RT	$S_0 \rightarrow S_1$	163 → 164	0.7065	2.13	581.79	0.0003
	$S_0 \rightarrow S_2$	162 → 164	0.7064	2.28	548.63	0.0003
	$S_0 \rightarrow S_3$	160 → 164	0.6106	2.52	492.60	0.0002
RG	$S_0 \rightarrow S_1$	159 → 160	0.7060	1.79	691.58	0.0009
	$S_0 \rightarrow S_2$	155 → 161	0.1255	2.60	476.55	0.5727
		159 → 161	0.5797			
	$S_0 \rightarrow S_3$	159 → 162	0.7018	2.69	460.23	0.0102

[a]*CI expansion coefficients for the main orbital transitions*.

The main orbital transitions were calculated using TD-DFT at the B3LYP/LanL2DZ level of theory and presented in table 5, Figs. 8 and 9. The oscillator strength of all singlet electronic transition of **RT** is insignificant, f < 0.01, indicating that **RT** is not a fluorescent compound [24]. The singlet electronic transition of **RG** is mainly contributed by the $S_0 \rightarrow S_2$ transitions with the strongest oscillation strength of 0.5727, and is composed of the transitions from MO-155→MO-161 and MO-159→MO-161. The transition from MO-155 to MO-161 does not cause the fluorescence. This is due to the fact that MO-155 belongs to receptor, but MO-161 belongs to fluorophore (Fig. 8), therefore the space distance between them is large, preventing the fluorescence. It is similar to the Förster Resonance Energy Transfer (FRET) - based sensors [25]. The transition from MO-159 to MO-161 is an important transition to cause the fluorescence in **RG**. Here, the PET process from receptor to fluorophore does not occur in **RG** because there is not any MO belonging to the receptor with energy level between MO-159 and MO-161 (Fig. 9).

NBO analysis results in table 6 provide more thorough insight into the bond properties and intermolecular orbital interaction, and therefore make clearer the fluorescent properties of **RT** and **RG**. The results further confirm the presence of spirolactam ring in **RT** molecule. The π-bond conjugated system of rhodamine fluorophore is broken at C10 atom and this causes the fluorescence quenching of **RT**. Meanwhile, the formation of guanidine ring and spirolactam ring-opening in **RG** restore the π-bond conjugated system of rhodamine fluorophore, causing the strong fluorescence in **RG**.

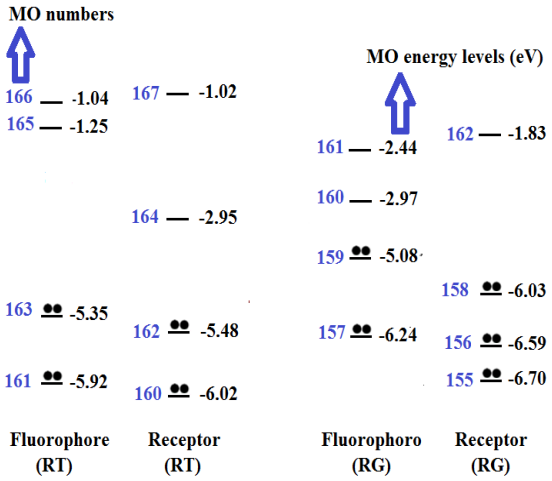

Figure 9: Frontier orbital energy diagram of free fluorophore, receptor and chemosimeter **RT** and **RG** (The energy levels are relative, not in proportion)

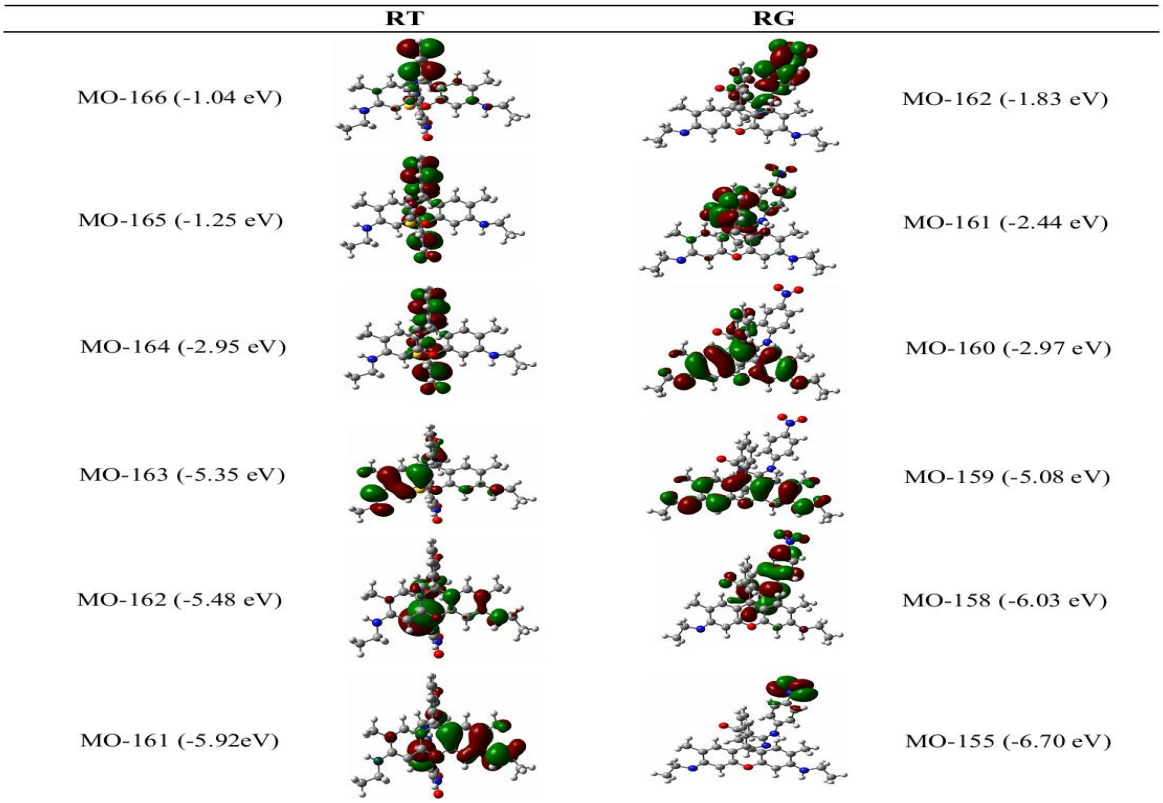

Figure 8: Molecular orbital plots of **RT** and **RG** at the B3LYP/LanL2DZ level. C, N, S, and H atoms denoted as gray, blue, yellow, and white atoms, respectively

Table 6: Significant second-order interaction energies ($E^{(2)}$, in kcal mol^{-1}) between donor and acceptor orbitals in **RT** and **RG** (at the B3LYP/LanL2DZ level of theory)

Donor NBO (*i*)	Acceptor NBO (*j*)	$E^{(2)}$	Donor NBO (*i*)	Acceptor NBO (*j*)	$E^{(2)}$
RT			**RG**		
π(C1–C6)	π*(C2–C3)	21.22	π(C1–C6)	π*(C2–C3)	20.68
π(C1–C6)	π*(C4–C5)	16.53	π(C1–C6)	π*(C4–C5)	16.45
π(C2–C3)	π*(C1–C6)	15.84	π(C2–C3)	π*(C1–C6)	16.67
π(C2–C3)	π*(C4–C5)	26.99	π(C2–C3)	π*(C4–C5)	28.09
π(C4–C5)	π*(C1–C6)	21.63	π(C4–C5)	π*(C1–C6)	22.26
π(C4–C5)	π*(C2–C3)	14.91	π(C4–C5)	π*(C2–C3)	18.04
π(C8–C9)	π*(C11–C12)	16.63	π(C4–C5)	π*(C9–C10)	17.75
π(C8–C9)	π*(C13–C14)	21.57	π(C8–C11)	π*(C9–C10)	16.20
π(C11–C12)	π*(C8–C9)	25.78	π(C8–C11)	π*(C12–C17)	17.79
π(C11–C12)	π*(C13–C14)	16.72	π(C9–C10)	π*(C4–C5)	13.65
π(C13–C14)	π*(C8–C9)	18.03	π(C9–C10)	π*(C8–C11)	17.79
π(C13–C14)	π*(C11–C12)	22.24	π(C9–C10)	π*(C13–C14)	15.54
			π(C12–N17)	π*(C8–C11)	12.39
			π(C12–N17)	π*(C13–C14)	10.65
			π(C13–C14)	π*(C9–C10)	17.95
			π(C13–C14)	π*(C12–N17)	17.69

4. CONCLUSION

The fluorescent chemodosimeter **RT** based on rhodamine derivative for detection of mercury ions was studied, including the synthesis process, characteristics and applications. The optimized geometry and the electron properties of **RT** and **RG** were identified at the B3LYP/LanL2DZ level of theory with a combination of AIM and NBO analysis. The obtained results showed that the presence of spirolactam ring in **RT** led to break the π-bond conjugated system of rhodamine fluorophore at C10 atom, causing the fluorescence quenching of **RT**. Meanwhile, the formation of guanidine ring and spirolactam ring-opening in RG restored the π-bond conjugated system of rhodamine fluorophore, leading to the strong fluorescence in **RG**. As a result, **RT** could be used as an *OFF-ON* fluorescent chemodosimeter for detection of Hg(II) ions.

Acknowledgment. *This research was funded by the Vietnam National Foundation for Science and Technology Development (NAFOSTED) under grant number 104.04-2014.35 (DTQ).*

REFERENCES

1. M. Y. Chae, A. W. Czarnik. *Mercury(II) and silver(I) indication in water via enhanced fluorescence signaling*, J. Am. Chem. Soc, **114(24)**, 9704-9705 (1992).
2. A. P. D. Silva, T. S. Moody and G. D. Wright. *Fluorescent PET (photoinduced electron transfer) sensors as potent analytical tools,* Analyst, **134(12)**, 2385-2393 (2009).
3. D. T. Quang, J. S. Kim. *Fluoro- and Chromogenic Chemodosimeters for Heavy Metal Ion Detection in Solution and Biospecimens*, Chem. Rev **110(10)**, 6280-6301 (2010).
4. H. S. Jung, J. H. Han, Y. Habata, C. Kang and J. S. Kim. *An iminocoumarin–Cu(II) ensemble-based chemodosimeter toward thiols*, Chem. Commun., **47**, 5142-5144 (2011).
5. J. S. Kim and D. T. Quang. *Calixarene-Derived Fluorescent Probes,* Chem. Rev., **107(9)**, 3780-3799 (2007).
6. S. H. Kim, H. S. Choi, J. Kim, S. J. Lee, D. T. Quang and J. S. Kim. *Novel Optical/Electrochemical Selective 1,2,3-Triazole Ring-Appended Chemosensor for the Al^{3+} Ion,* Org. Lett., **12(3)**, 560-563 (2010).
7. M. Kumar, N. Kumar, V. Bhalla, H. Singh, P. R. Sharma and T. Kaur. *Naphthalimide Appended Rhodamine Derivative: Through Bond Energy Transfer for Sensing of Hg^{2+} Ions*, Org. Lett., **13(6)**, 1422-1425 (2011).

8. M. H. Lee, T. V. Giap, S. H. Kim, Y. H. Lee, C. Kang, J. S. Kim. *A novel strategy to selectively detect Fe(III) in aqueous media driven by hydrolysis of arhodamine 6G Schiff base*, Chem. Commun., **46(9)**, 1407-1409 (2010).
9. D. T. Quang, N. V. Hop, N. D. Luyen, H. P. Thu, D. Y. Oanh, N. K. Hien, N. V. Hieu, M. H. Lee, J. S. Kim. *A new fluorescent chemosensor for Hg^{2+} in aqueous solution*, Luminescence, **28**, 222-225 (2013).
10. N. K. Hien, P. T. Quy, N. T. Trung, V. Vien, D. V. Khanh, N. T. A. Nhung, D. T. Quang. *A dansyl-diethylenetriamine-thiourea conjugate as a fluorescent chemodosimeter for Hg^{2+} ions in water media*, Chem. Lett., **43**, 1034-1036 (2014).
11. N. K. Hien, N. C. Bao, N. T. A. Nhung, N. T. Trung, P. C. Nam, T. Duong, J. S. Kim, D. T. Quang. *A highly sensitive fluorescent chemosensor for simultaneous determination of Ag(I), Hg(II), and Cu(II) ions: Design, synthesis, characterization and application*, Dyes. Pigm., **116**, 89-96 (2015).
12. P. T. Quy, N. K. Hien, N. C. Bao, D. T. Nhan, D. V. Khanh, N. T. A. Nhung, T. Q. Tung, N. D. Luyen, D. T. Quang. *A new rhodamine-based fluorescent chemodosimeter for mercuric ions in water media*, Luminescence, **30(3)**, 325-329 (2015).
13. N. K. Hien, N. T. A. Nhung, H. Q. Dai, N. T. Trung, D. T. Quang. *A fluorescent sensor based on dansyl-diethylenetriamine-thiourea conjugate: design, synthesis, characterization, and application*, Vietnam Journal of Chemistry, **53(5e)**, 541-547 (2015).
14. J. Yang, Z. Lei, Z. Peng. *A rhodamine B-based fluorescent sensor toward highly selective mercury (II) ions detection*, Talanta, **150**, 14-19 (2016).
15. C. Khwanchanok, C. Nathawut, Y. Peerada, T. Panumart. *A highly selective 'turn-on' fluorescent sensor for Zn^{2+} based on fluorescein conjugates*, Tetrahedron Lett., **57(10)**, 1146-1149 (2016).
16. A. D. Becke. *Density-functional thermochemistry. IV. A new dynamical correlation functional and implications for exact-exchange mixing*, J. Chem. Phys., **104**, 1040-1046 (1996).
17. A. D. Becke. *Density-functional thermochemistry. III. The role of exact exchange*, J. Chem. Phys., **98**, 5648-5652 (1993).
18. C. Lee, W. Yang, R. G. Parr. *Development of the Colle-Salvetti correlation-energy formula into a functional of the electron density*, Phys. Rev B**37**, 785-789 (1988).
19. M. J. Frisch, et al., Gaussian 09, Revision E.01, Gaussian, Inc; Wallingford, CT (2009).
20. R. F. W. Bader. *A quantum theory of molecular structure and its applications*, Chem. Rev., **91(5)**, 893-928 (1991).
21. M. J. Frisch et al. AIM 2000, designed by Friedrich Biegler-König. University of Applied Sciences. Germany: Bielefeld (2000).
22. D. N. Adhikesavalu, D. Mastropaolo, A. Camerman, N. Camerman. *Two rhodamine derivatives: 9-[2-(ethoxycarbonyl)phenyl]-3,6-bis(ethylamino)-2,7-dimethylxanthylium chloride monohydrate and 3,6-diamino-9-[2-(methoxycarbonyl)phenyl]xanthylium chloride trihydrate*, Acta. Cryst C**57**, 657-659 (2001).
23. J. C. Miller and J. N. Miller. *Statistics for analytical chemistry*, second ed. Chichester, England: Ellis Horwood Limited (1998).
24. K. Saita, M. Nakazono, K. Zaitsu, S. Nanbo, H. Sekiya, *Theoretical Study of Photophysical Properties of Bisindolylmaleimide Derivatives*, J. Phys. Chem.B., **113**, 8213-8220 (2009).
25. S. A. Hussain et al. *An introduction to fluorescence resonance energy transfer (FRET).* Science Journal of Physics Article ID sjp-268, 4 Pages, Doi: 10.7237/sjp/268 (2012).

Corresponding author: **Duong Tuan Quang**
College of Education - Hue University, Hue City, Vietnam
No. 34, Le Loi, Hue City, Thua Thien Hue
E-mail: duongtuanquang@dhsphue.edu.vn; Telephone number: 0914050126.